Geophysical Research Letters

RESEARCH LETTER
10.1029/2023GL102881

Vertical-Slice Ocean Tomography With Seismic Waves

Jörn Callies[1], Wenbo Wu[1,2], Shirui Peng[1], and Zhongwen Zhan[1]

[1]California Institute of Technology, Pasadena, CA, USA, [2]Wood Hole Oceanographic Institution, Woods Hole, MA, USA

Key Points:

- Seismic *T* waves at different frequencies sample different parts of the water column
- Frequency-dependent travel time changes between repeating earthquakes constrain the depth-dependent temperature change between the events
- These data reveal the vertical structure of temperature anomalies produces by equatorial waves, mesoscale eddies, and decadal warming

Supporting Information:

Supporting Information may be found in the online version of this article.

Correspondence to:

J. Callies,
jcallies@caltech.edu

Citation:

Callies, J., Wu, W., Peng, S., & Zhan, Z. (2023). Vertical-slice ocean tomography with seismic waves. *Geophysical Research Letters*, *50*, e2023GL102881. https://doi.org/10.1029/2023GL102881

Received 3 FEB 2023
Accepted 5 APR 2023

Abstract Seismically generated sound waves that propagate through the ocean are used to infer temperature anomalies and their vertical structure in the deep East Indian Ocean. These *T* waves are generated by earthquakes off Sumatra and received by hydrophone stations off Diego Garcia and Cape Leeuwin. Between repeating earthquakes, a *T* wave's travel time changes in response to temperature anomalies along the wave's path. What part of the water column the travel time is sensitive to depends on the frequency of the wave, so measuring travel time changes at a few low frequencies constrains the vertical structure of the inferred temperature anomalies. These measurements reveal anomalies due to equatorial waves, mesoscale eddies, and decadal warming trends. By providing direct constraints on basin-scale averages with dense sampling in time, these data complement previous point measurements that alias local and transient temperature anomalies.

Plain Language Summary Taking up almost all of the excess heat trapped on Earth by anthropogenic greenhouse gases, the ocean exerts a key control on our warming climate. Despite progress, tracking that heat remains an observational challenge. This study presents new measurements of ocean warming by making use of sound waves that are generated by earthquakes and propagate long distances through the ocean. These sound waves propagate faster in warmer seawater, so they arrive slightly earlier if warming has occurred. In this study, we measure such changes in arrival time at different frequencies—or pitches—that are sensitive to different parts of the water column, so warming in the upper ocean can be distinguished from warming in the deep ocean.

1. Introduction

The ocean is warming in response to accumulating greenhouse gases in the atmosphere, and its heat capacity dominates the climate system's thermal inertia. While the warming has been most pronounced in the surface ocean, heat transfer to the deep ocean importantly slows the climate change experienced at the surface (e.g., Gregory, 2000; Hansen et al., 1981; Held et al., 2010; Kostov et al., 2014). Roemmich et al. (2015), for example, estimated from Argo floats that the top 0.5 km of the global ocean warmed at a rate of 5 $mKyr^{-1}$ between 2006 and 2013, whereas the layer between 0.5 and 2 km warmed at a rate of 2 $mKyr^{-1}$. Had the heat not been transferred below 0.5 km depth, the top 0.5 km would have warmed more than twice as rapidly (excluding feedbacks with the atmosphere and radiative transfer). It is thus important to constrain the heat transfer to the deep ocean. Because this transfer is achieved by processes that depend on uncertain parameterizations in climate models (the overturning circulation, mesoscale eddies, and diapycnal mixing), strong observational constraints are crucial.

It remains an observational challenge to isolate the small-amplitude and large-scale climate signal in the presence of much larger-amplitude but local fluctuations due to mesoscale eddies, internal waves, and other oceanic transients. To 2 km depth and since the mid-2000s, Argo floats have provided unprecedented coverage of the world ocean. Even with currently about 4,000 floats, however, the Argo array still aliases mesoscale eddies, and regional estimates of warming rates remain uncertain (e.g., Dushaw, 2019; Wunsch, 2016; Figure 1a). Additionally, and maybe more glaringly, Core Argo floats do not sample half of the ocean's volume: that below 2 km depth. While the Deep Argo array is expanding (e.g., Johnson et al., 2020; Roemmich et al., 2019), the extant record is short and limited to a few regions. Estimates of temperature change below 2 km rely heavily on sparse hydrographic sections that are sampled about once a decade (e.g., Desbruyères et al., 2016, 2017; Purkey & Johnson, 2010; Roemmich & Wunsch, 1984; Volkov et al., 2017; Figure 1a). State estimates constrain such changes by combining available observations with an ocean model (e.g., Wunsch & Heimbach, 2007), but the possibility of model error and the lack of an uncertainty estimate make it difficult to assess how reliable such estimates are. For example, Wunsch and Heimbach (2014) inferred widespread cooling of the abyssal ocean using the ECCO (v4r1) state estimate (relative to an assumed and corrected initial state), whereas direct estimates from

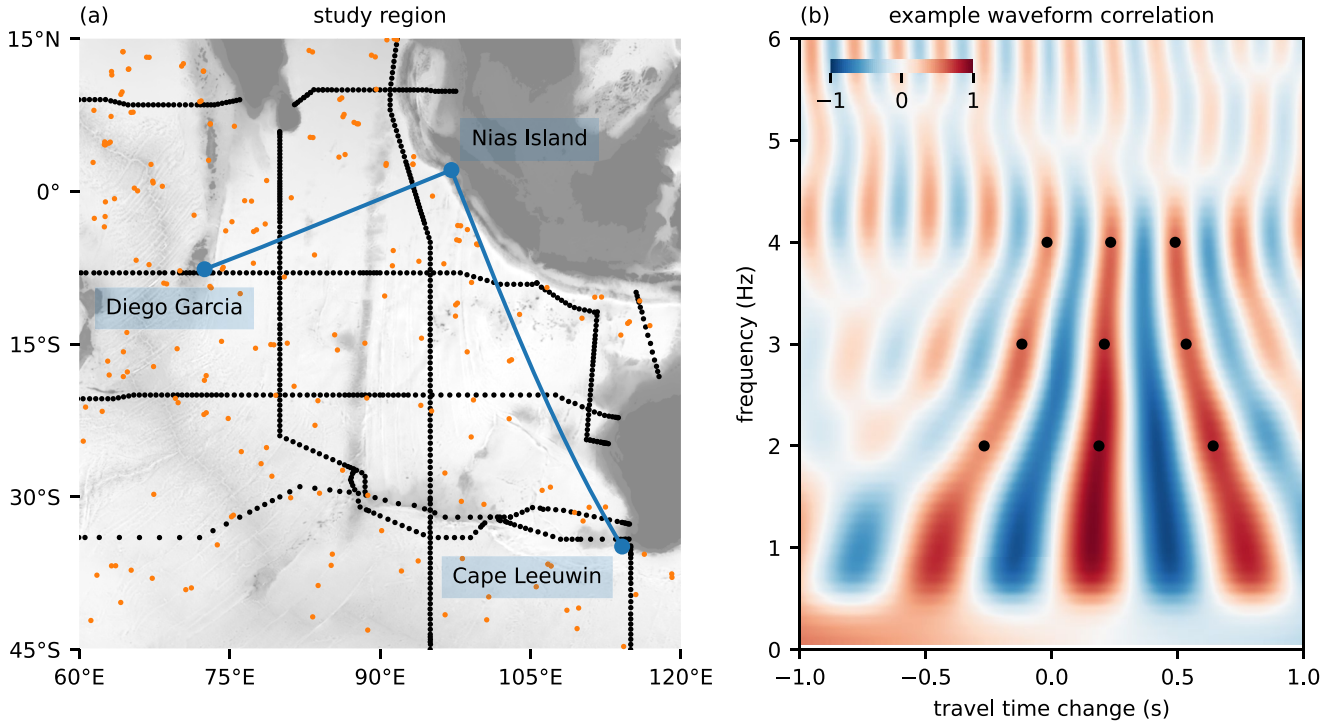

Figure 1. Study region and example measurement of the frequency-dependent travel time change. (a) Locations of the Nias Island earthquakes and the hydrophone receivers at Diego Garcia and Cape Leeuwin. Also shown are the locations of all Argo profiles collected during the 10 days following the 2005-03-28 Nias–Simeulue earthquake (orange dots) and the WOCE hydrographic sections (black dots). (b) Frequency-dependent waveform correlation function for the event pair 2005-04-12 09:56:39, 2008-10-11 12:32:32. The black dots indicate measurements for the central maximum as well as the two adjacent maxima that are used for cycle skipping correction (not needed for this pair). An origin time correction of 4.28 s was applied based on the waveforms received at land station PSI.

repeat hydrographic sections tend to indicate a dominance of warming (e.g., Desbruyères et al., 2017; Purkey & Johnson, 2010). Clearly, better observational constraints are needed.

Recently, Wu et al. (2020) demonstrated that sound waves generated by earthquakes, so-called *T* waves, can be used to constrain basin-scale temperature change in the deep ocean. These measurements are based on the idea of "ocean acoustic tomography," which was originally proposed by Munk and Wunsch (1979) and successfully demonstrated at both planetary (Munk & Forbes, 1989) and basin scales (The ATOC Consortium, 1998). *T* waves propagate faster in warmer water, so changes in the average temperature encountered by these waves can be detected as changes in their travel time. The use of sound waves produced by earthquakes eliminates the need to deploy synthetic sound sources. Wu et al. used the seismic station DGAR on Diego Garcia to receive *T* waves generated 2900 km away by earthquakes near Nias Island off Sumatra (Figure 1a). To remove uncertainties in the source location and timing, repeating earthquakes were employed to extract the change in travel time between two events. A key advantage of such acoustic measurements over point measurements is that they intrinsically average the temperature change along the sound waves' path and therefore suffer much less from spatial aliasing.

In an accompanying manuscript (hereafter referred to as W23), we show that Comprehensive Nuclear-Test-Ban Treaty Organization (CTBTO) hydrophones are more sensitive *T*-wave receivers than land stations like DGAR, which allows the detection of smaller earthquakes at the CTBTO station H08 off Diego Garcia than is possible with DGAR data. This use of CTBTO data improves the time resolution of the inferred deep-ocean temperature change between Nias Island and Diego Garcia. In W23, we further use Nias Island *T*-waves received at the CTBTO station H01 off Cape Leeuwin to infer a time series of temperature change averaged along this 4,400 km section extending into the extratropical ocean (Figure 1a).

Here, we make use of an additional advantage of the crisp arrivals of *T* waves in CTBTO hydrophone records: that changes in the travel time can be measured reliably at a number of different frequencies (Figure 1b, Section 2). Because *T* waves at different frequencies are sensitive to different parts of the water column, this frequency dependence in the travel time change can be used to constrain the vertical structure of the temperature change

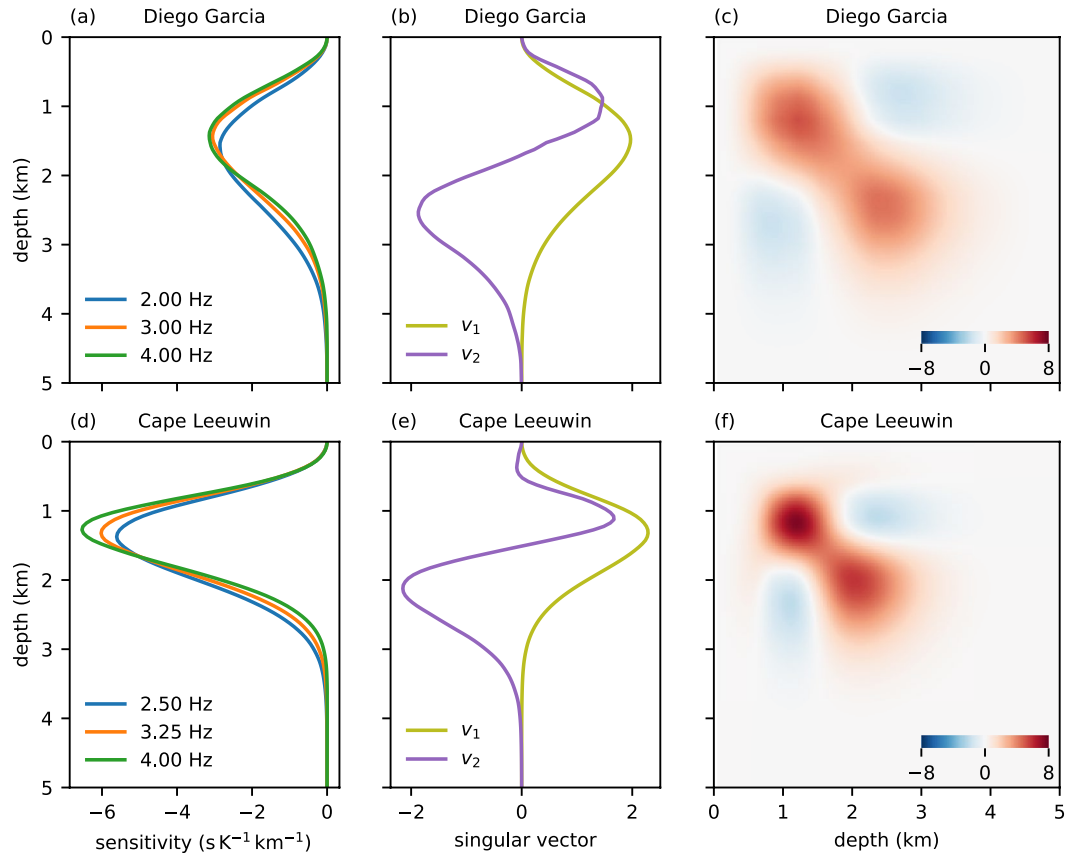

Figure 2. Sensitivity kernels and inference of vertical structure. Shown are (a, d) the range-averaged sensitivity kernels at different frequencies, (b, e) the first two singular vectors obtained from these range-averaged sensitivity kernels, and (c, f) the resolution matrices of the singular value decomposition inversion employing the first two singular vectors. All these are shown for the path to Diego Garcia (top row) and that to Cape Leeuwin (bottom row).

(Figure 2; cf., Munk & Wunsch, 1983; Shang, 1989). This approach is similar to that employed in remote sensing of the atmosphere (e.g., Fu et al., 2004), except that acoustic rather than electromagnetic waves are used.

A similar vertical-slice tomography scheme has been developed for acoustic measurements with synthetic sources (e.g., Munk & Wunsch, 1979, 1982; Munk et al., 1995), but it has not been realized at a basin scale. The sources employed in the Acoustic Thermometry of Ocean Climate (ATOC) experiment had frequencies centered on 75 Hz and were effectively point sources at precisely known locations, allowing for a convenient eigenray description of the propagation from source to receiver. These rays have a known geometry and, under certain circumstances, can be resolved and identified in arrival patterns (Cornuelle et al., 1993; Spiesberger et al., 1980; The ATOC Consortium, 1998; The Ocean Tomography Group, 1982; Worcester et al., 1999). Relative changes in the arrival times of different rays can then be used to infer the vertical structure of temperature change, most easily in the range average. For example, the arrival time of steep rays that sample the surface mixed layer undergo a larger seasonal cycle than near-axial rays that are confined to the thermocline and deep ocean. On the bottom-mounted receivers used in ATOC, however, only relatively steep rays could be resolved and identified, and the information on the vertical structure of the temperature field was limited (Dushaw, 1999; Dushaw et al., 2009).

The propagation and arrival patterns of *T* waves are more complicated (e.g., Okal, 2008), but information on the vertical structure of the temperature change can still be extracted. Sensitivity kernels quantify how the arrival time changes in response to a temperature perturbation anywhere along the path and anywhere in the water column (Figure 2; Wu et al., 2020). Consistent with expectations from simplified modal calculations (Figure S1 in Supporting Information S1), these range-averaged sensitivity kernels shift upward in the water column for increasing frequencies (Figure 2). A surface-intensified warming, for example, produces a larger reduction in travel time at high frequencies than at low frequencies. We use this frequency dependence to estimate a rough vertical structure of the range-averaged deep temperature anomalies. We find that the inferred structure of the

anomalies along the two sections matches expectations based on the dynamics that produce the anomalies and is in general agreement with previous estimates, although the *T*-wave data tends to show stronger anomalies and more reliably captures perturbations due to mesoscale eddies (Section 3).

2. Inferring Vertical Structure

The starting point for the inference of vertical structure in the temperature anomalies are the time series of travel time anomalies at a few different low frequencies, constructed from a total of 11,479 repeating pairs that arise from 3,457 earthquakes in 2005–2018 (Figure 1b; W23). We choose 2.00, 3.00, and 4.00 Hz for the path to Diego Garcia and 2.50, 3.25, and 4.00 Hz for the path to Cape Leeuwin. A slightly higher minimum frequency is used for the latter path because 2.00 Hz *T* waves are less consistently received at Cape Leeuwin than at Diego Garcia. Measurements at higher frequencies are not reliable because the waveform correlation drops markedly beyond 4 Hz (e.g., Figure 1b). For each frequency, we apply a Gaussian filter with width 0.5 Hz centered on that frequency before calculating the correlation function between the *T*-wave arrivals of an event pair, as described in W23. How these time series are obtained from measured travel time differences between repeating events is described in Text S1 in Supporting Information S1, and the cycle skipping corrections that are applied to the measurements are described in Text S2 in Supporting Information S1.

To turn the time series of travel time anomalies at different frequencies into an estimate of the evolving vertical structure of temperature anomalies, we perform a singular value decomposition (SVD) of the range-integrated sensitivity kernels (Figure 2). The problem is severely under-determined, so we can only hope to obtain a coarse estimate of the vertical temperature structure. Let $\mathbf{K}$ denote the matrix whose three rows contain the range-integrated sensitivity kernels at the three frequencies, discretized to a $\Delta z = 50$ m grid. Then, at each event time t, we would like to invert $\boldsymbol{\tau}(t) = \mathbf{K}\boldsymbol{T}(t)\Delta z$ for $\boldsymbol{T}(t)$, where $\boldsymbol{\tau}(t)$ contains the *T*-wave travel time anomalies at the three frequencies, and $\boldsymbol{T}(t)$ contains the range-averaged temperature anomaly profiles on the same grid as the kernels. The SVD $\mathbf{K} = \mathbf{U}\boldsymbol{\Lambda}\mathbf{V}^{\mathrm{T}}$ yields the singular values $\lambda_1 = 2.6$ sK^{-1} km^{-1}, $\lambda_2 = 0.21$ sK^{-1} km^{-1}, and $\lambda_3 = 0.022$ sK^{-1} km^{-1} for the path to Diego Garcia and $\lambda_1 = 4.6$ sK^{-1} km^{-1}, $\lambda_2 = 0.30$ sK^{-1} km^{-1}, and $\lambda_3 = 0.012$ sK^{-1} km^{-1} for the path to Cape Leeuwin (see Text S1 in Supporting Information S1 for details). The rapid decay in the singular values is a result of the similarity of the sensitivity kernels at the chosen frequencies, that is, their being nearly linearly dependent. Small singular values amplify errors (we only know the estimate $\tilde{\boldsymbol{\tau}}$, not the true $\boldsymbol{\tau}$), so a common trade-off must be made between resolution and precision. We choose to retain the first two singular vectors to obtain coarse vertical resolution with acceptable uncertainty: $\tilde{\boldsymbol{T}}_2(t) = h^{-1}\mathbf{V}_2\boldsymbol{\Lambda}_2^{-1}\mathbf{U}_2^{\mathrm{T}}\tilde{\boldsymbol{\tau}}(t)$, where $\mathbf{U}_2$ and $\mathbf{V}_2$ consist of the first two columns of $\mathbf{U}$ and $\mathbf{V}$, respectively, $\boldsymbol{\Lambda}_2$ is the diagonal matrix containing λ_1 and λ_2, and $h = 5$ km is a fixed reference depth. The estimate $\tilde{\boldsymbol{T}}_2(t)$ is then related to the true temperature field $\boldsymbol{T}(t)$ by $\tilde{\boldsymbol{T}}_2(t) = h^{-1}\mathbf{V}_2\mathbf{V}_2^{\mathrm{T}}\boldsymbol{T}(t)\Delta z + h^{-1}\mathbf{V}_2\boldsymbol{\Lambda}_2^{-1}\mathbf{U}_2^{\mathrm{T}}[\tilde{\boldsymbol{\tau}}(t) - \boldsymbol{\tau}(t)]$. In the absence of errors in $\tilde{\boldsymbol{\tau}}(t)$, the estimate $\tilde{\boldsymbol{T}}_2(t)$ is a projection of the true state $\boldsymbol{T}(t)$ onto the first two singular vectors, and the resolution matrix $\mathbf{V}_2\mathbf{V}_2^{\mathrm{T}}$ determines to what degree features can be resolved by the available data. For both paths, only features between about 0.5 and 3 km depth can be captured, and the depth resolution is no better than about 1 km (Figure 2). The projection coefficients are estimated from the data as $\tilde{\boldsymbol{c}}_2(t) = h^{-1}\mathbf{V}_2^{\mathrm{T}}\tilde{\boldsymbol{T}}_2(t)\Delta z = h^{-1}\boldsymbol{\Lambda}_2^{-1}\mathbf{U}_2^{\mathrm{T}}\tilde{\boldsymbol{\tau}}(t)$, with which the reconstructed temperature profile is the linear combination $\tilde{\boldsymbol{T}}_2(t) = \mathbf{V}_2\tilde{\boldsymbol{c}}_2(t)$. (Note that the prior covariances for inferring $\tilde{\boldsymbol{\tau}}(t)$ from the travel time changes between repeating events are chosen such that the three components of $\tilde{\boldsymbol{c}}(t) = h^{-1}\boldsymbol{\Lambda}^{-1}\mathbf{U}^{\mathrm{T}}\tilde{\boldsymbol{\tau}}(t)$ are uncorrelated. Any phase relations between them therefore arise entirely from the data. Details are given in Text S1 in Supporting Information S1).

Taking this SVD approach to inversion, we feign complete ignorance about the vertical structure of the range-averaged temperature anomalies. The inversion uses neither constraints from the physics that govern the temperature field nor prior information, say from previous measurements or model simulations. In particular, the inversion knows nothing of the typically strong surface intensification of temperature anomalies, which entails that inverted temperature anomalies tend to reach too deep and that upper-ocean anomalies can produce spurious oppositely signed deep anomalies (Figures S6 and S7 in Supporting Information S1). We nevertheless choose this agnostic approach to illustrate most simply what information is contained in the *T*-wave data. Future work should combine this information from seismic data with prior information and other observations.

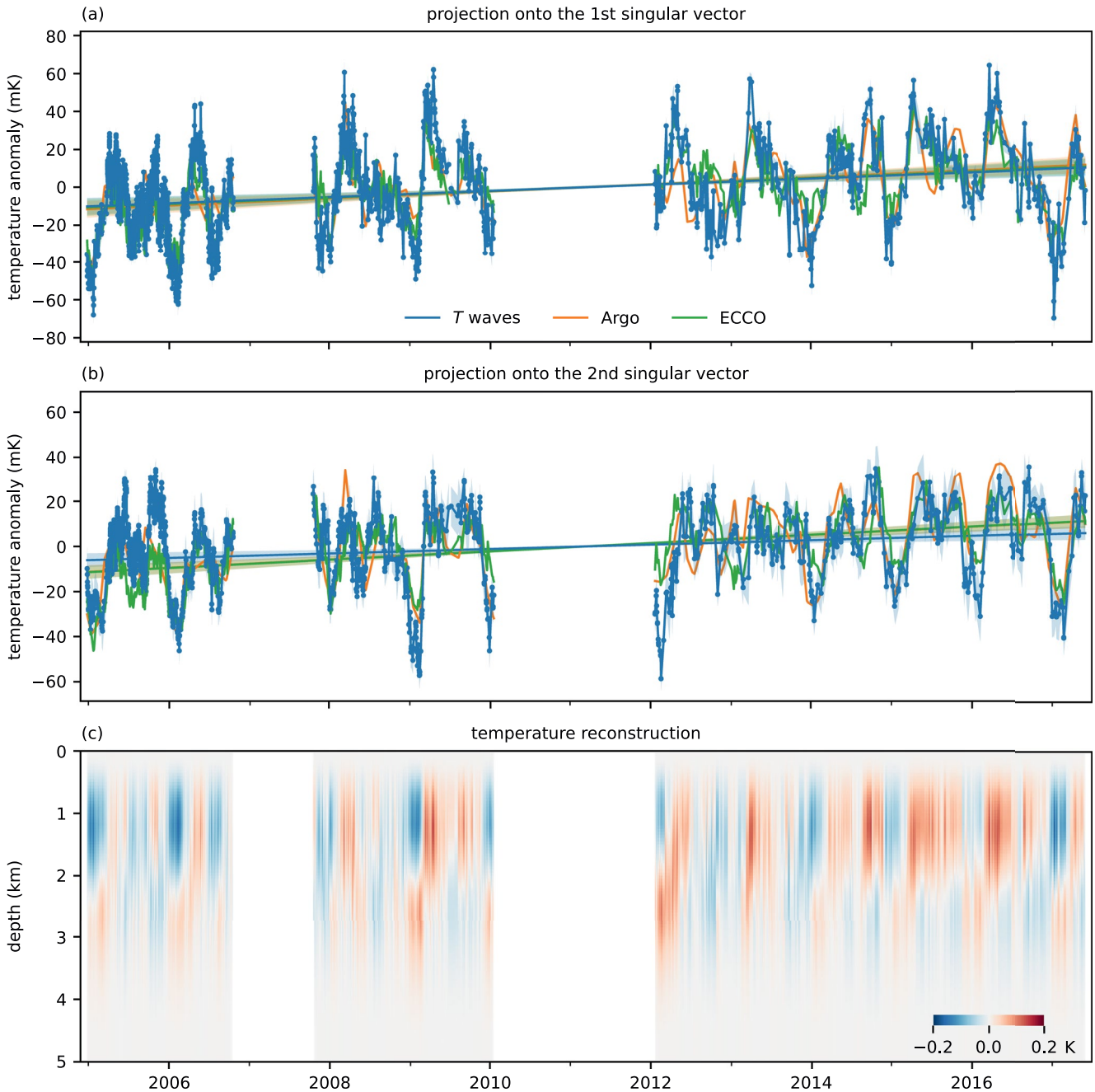

Figure 3. Inferred temperature anomalies for the path to Diego Garcia. Shown are (a, b) the projections onto the first two singular vectors $\tilde{c}_2$ for the T-wave data and two reference products and (c) the singular value decomposition reconstruction of the range-averaged temperature anomaly profile $\tilde{T}_2$ obtained from the T-wave data. Each dot in (a, b) corresponds to an estimate at an event time, and the shading indicates $\pm 2\sigma$ confidence intervals around these estimates. Also shown are the estimated decadal trends of the projection coefficients $\tilde{c}_2$, including their $\pm 2\sigma$ uncertainties.

3. Time Series

Time series of the temperature profiles projected onto the first two singular vectors show prominent seasonal and sub-seasonal variations, as well as significant decadal trends for the path to Diego Garcia (Figures 3a, 3b, 4a, and 4b; Table 1). The first singular vectors have a similar shape as the kernels themselves, so their coefficients represent a weighted average of the deep temperature anomalies, with the weighting peaked at 1.5 and 1.3 km for the paths to Diego Garcia and Cape Leeuwin, respectively (Figures 2b and 2e). The second singular vectors have

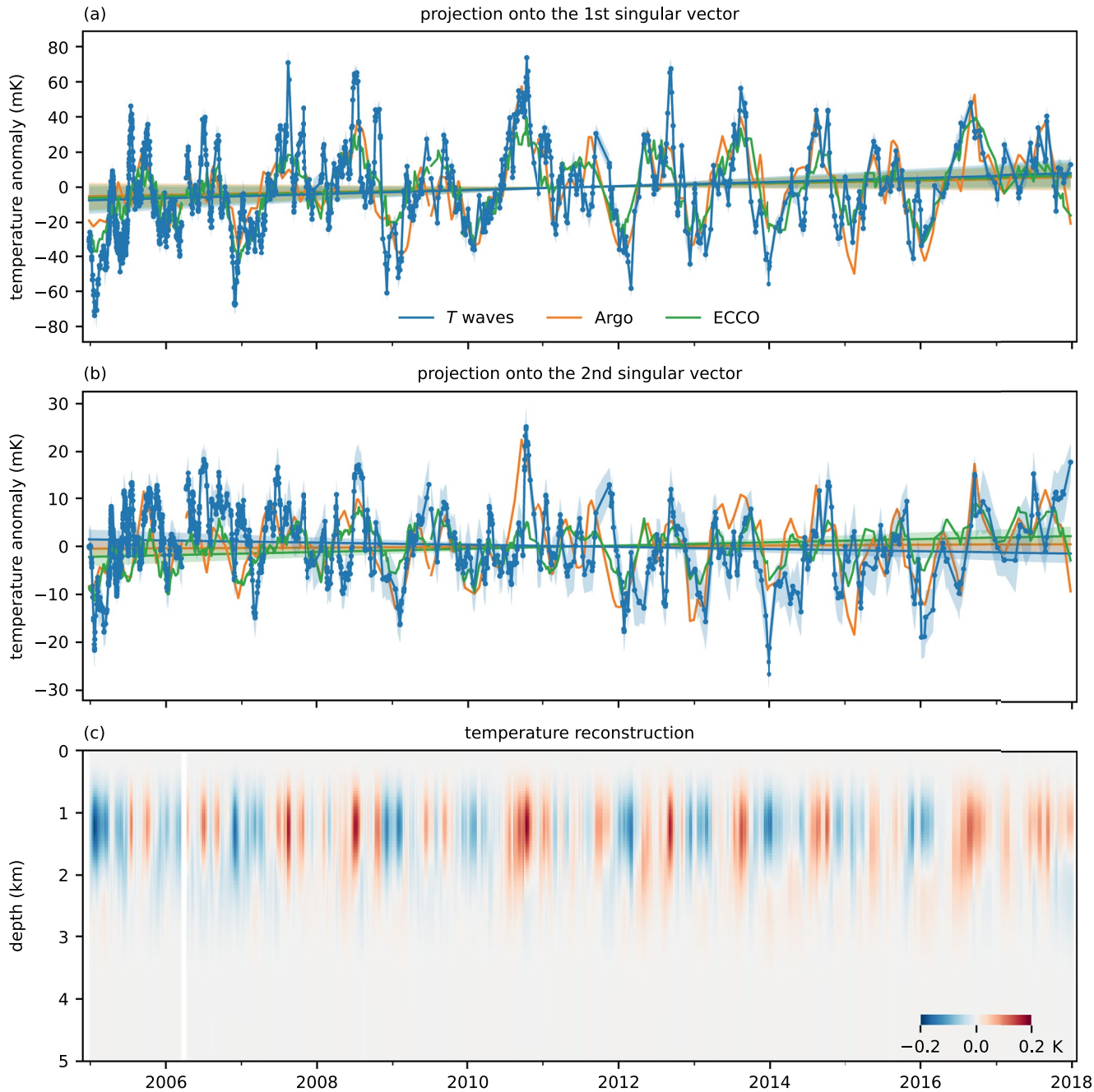

Figure 4. Inferred temperature anomalies for the path to Cape Leeuwin. Shown are (a, b) the projections onto the first two singular vectors $\tilde{\boldsymbol{c}}_2$ for the *T*-wave data and two reference products and (c) the singular value decomposition reconstruction of the range-averaged temperature anomaly profile $\tilde{\boldsymbol{T}}_2$ obtained from the *T*-wave data. Each dot in (a, b) corresponds to an estimate at an event time, and the shading indicates $\pm 2\sigma$ confidence intervals around these estimates. Also shown are the estimated decadal trends of the projection coefficients $\tilde{\boldsymbol{c}}_2$, including their $\pm 2\sigma$ uncertainties.

nodes at 1.7 and 1.5 km for the two paths, so the projection onto them is more sensitive to where in the water column the anomalies are located.

These projections inferred from *T*-wave travel time anomalies show general agreement with previous products. We compare our estimates to monthly interpolated Argo data (Roemmich & Gilson, 2009) and daily ECCO state estimate data (v4r4; ECCO Consortium, 2021; Forget et al., 2015). Using the sensitivity kernels, we infer travel time anomalies from the temperature anomalies of these products, interpolate those onto our event times, and subsequently treat them in the same way as the *T*-wave anomalies.

Table 1
Trends and Amplitudes of the Annual and Semi-Annual Signals Inferred From T-Wave Data and Previous Products

		Trends (mKyr^{-1})		12 month (mK)		6 month (mK)	
		1	2	1	2	1	2
Diego Garcia	*T* waves	$+1.6 \pm 0.7$	$+1.1 \pm 0.5$	15 ± 4	12 ± 4	15 ± 4	11 ± 4
	Argo	$+1.9 \pm 0.7$	$+1.8 \pm 0.5$	9 ± 4	9 ± 1	12 ± 4	11 ± 2
	ECCO	$+1.7 \pm 0.7$	$+1.9 \pm 0.5$	8 ± 4	8 ± 2	11 ± 3	11 ± 3
Cape Leeuwin	*T* waves	$+1.1 \pm 1.2$	-0.2 ± 0.3	20 ± 5	5 ± 5	3 ± 5	2 ± 5
	Argo	$+0.8 \pm 1.2$	$+0.1 \pm 0.3$	19 ± 5	5 ± 3	3 ± 4	3 ± 1
	ECCO	$+1.0 \pm 1.2$	$+0.3 \pm 0.3$	16 ± 5	3 ± 3	3 ± 4	3 ± 2

Note. These parameters are estimated for the temperature projections onto the first two singular vectors (columns labeled 1 and 2). All uncertainties are given as $\pm 2\sigma$.

For the path to Diego Garcia, seasonal and sub-seasonal variations in both these projections tend to line up (Figures 3a and 3b), indicating that the vertical structure inferred from the *T*-wave data is broadly consistent with these previous estimates. There are notable exceptions. The anomalies inferred from the *T*-wave data are stronger on average, particularly in the projection onto the first singular vector (Figure 3a, Table 1). The projection onto the second singular vector (Figure 3b) is more positive for the Argo product than for the *T*-wave data in the latter part of the time series, and it is less negative for ECCO than for the *T*-wave data in the early part of the time series, producing a stronger decadal trend in both previous products than inferred from the *T*-wave data (Table 1).

For the path to Cape Leeuwin, the seasonal variations in both projections are similar between those inferred from *T*-wave data and those from previous products (Figures 4a and 4b). In contrast to the equatorial path to Diego Garcia, the annual signal here is much stronger than the semi-annual signal (Table 1). The *T*-wave data produces sizable spikes with a duration on the order of a month, which are typically missed by previous data (Figures 4a and 4b; Figures S7 and S9 in Supporting Information S1). As discussed in W23, we interpret these spikes as resulting from mesoscale eddies traversing the path, most importantly those shed by the Leeuwin Current. The temperature anomalies of these eddies are largely confined to the thermocline (e.g., Fieux et al., 2005), which is consistent with the anomalies in the two projections appearing in phase. At times, these eddies happen to be captured by Argo floats (e.g., 2005-10 and 2010-10), but they are more typically missed, as expected from the Argo float coverage (Figure 1). ECCO does not capture mesoscale eddies because it has too low a horizontal resolution. The overall stronger variability along this path to Cape Leeuwin implies that decadal trends are more uncertain (Table 1), although the uncertainties in the estimation from the three data sources are not independent.

Time series of the temperature reconstruction $\tilde{\boldsymbol{T}}_2$ illustrate the information on the vertical structure contained in the *T*-wave data. On the path to Diego Garcia, the inferred temperature anomalies are strongest in the upper 2 km but reach substantially below this depth (Figure 3c). It cannot be inferred from the data whether these abyssal anomalies are real or whether they arise from the insufficient vertical resolution. (See Figures S6, S7, S8, and S9 in Supporting Information S1 for projections of Argo and ECCO data onto the first two singular vectors.). Nevertheless, the anomalies display an upward phase propagation that is expected for long surface-generated equatorial waves that have a downward energy flux (e.g., Luyten & Roemmich, 1982; McPhaden, 1982; Philander, 1978; Reppin et al., 1999; Wunsch, 1977). This upward phase propagation is not apparent on the extratropical path to Cape Leeuwin (Figure 4c), where the inferred anomalies are more strongly confined to above 2 km depth, consistent with mesoscale thermocline eddies.

In interpreting these results, it should be kept in mind that the sensitivity kernels are based on two-dimensional numerical simulations of the wave propagation from the source to the receiver (Wu et al., 2020). These simulations depend, albeit not sensitively, on assumptions about the thickness and properties of sediment layers and on the neglect of off-geodesic effects. There is therefore representational uncertainty in our estimates of temperature anomalies and their vertical structure arising from uncertainty in the kernels. More work is needed to better understand these effects.

4. Conclusions

The data presented here demonstrate that changes in *T*-wave travel times contain information on the vertical structure of the temperature anomalies encountered by these waves along their paths. This information can be extracted from travel time anomalies at a few low frequencies even though the sensitivity kernels at these frequencies have similar vertical structures (Figure 2).

We here illustrated this vertical structure using a simple SVD inversion. In the future, the *T*-wave data should be combined with Argo and ship-based hydrographic data, either using a relatively simple mapping as typically employed for Argo data or using state estimation as in ECCO, which also allows one to incorporate additional constraints, for example, from altimetry and gravitometry. *T* waves offer constraints on the large-scale temperature changes that are complementary to previous data. They intrinsically average in space, so they do not miss mesoscale eddies like the Argo array does. They offer a dense sampling in time, which is important even for large-scale averages that still contain sizable anomalies induced by equatorial waves and mesoscale eddies. *T* waves offer constraints on the ocean below 2 km depth, which has been sparsely sampled in space and time by ship-based hydrographic surveys. The vertical resolution obtained from *T* waves is relatively coarse, but they nevertheless constrain the vertical structure of the large-scale temperature anomalies.

In the present work, we restricted ourselves to low frequencies because the waveform correlation drops substantially at higher frequencies (Figure 1b) and travel time changes cannot be extracted confidently. The *T*-wave signals have plenty of power at these higher frequencies, so noise is unlikely to be the problem. Instead, we speculate that the higher-frequency signals contain multiple vertical acoustic modes. The modes become more confined in the vertical as the frequency increases, so more modes escape interaction with the bottom and subsequent attenuation. Different modes experience different time shifts, so the waveform correlation drops if multiple modes contribute substantially. If this interpretation is correct, much more detailed information on the vertical structure could be extracted if we were able to separate the modes in the received signal, for example, using a vertical hydrophone array (D'Spain et al., 2001). Deploying such arrays is routine, so future *T*-wave measurements could yield much stronger constraints on the vertical structure of the ocean's large-scale temperature variability.

Disclaimer

The views expressed in the paper are those of the authors and do not necessarily represent those of the CTBTO.

Data Availability Statement

The IMS hydrophone data are available directly from the CTBTO upon request and signing a confidentiality agreement to access the virtual Data Exploitation Centre (vDEC). All seismic data were downloaded through the IRIS Data Management Center (https://service.iris.edu/), including the seismic networks II (GSN; https://doi.org/10.7914/SN/II), MY, PS, and GE (https://doi.org/10.14470/TR560404). The Global Seismographic Network (GSN) is a cooperative scientific facility operated jointly by the Incorporated Research Institutions for Seismology (IRIS), the United States Geological Survey (USGS) and the National Science Foundation (NSF), under Cooperative Agreement EAR-1261681. The processing code is available at https://github.com/joernc/SOT.

Acknowledgments
This material is based upon work supported by the Resnick Sustainability Institute and by the National Science Foundation under Grant OCE-2023161.

References

Behringer, D., Birdsall, T., Brown, M., Cornuelle, B., Heinmiller, R., Knox, R., et al. (1982). A demonstration of ocean acoustic tomography. *Nature*, *299*(5879), 121–125. https://doi.org/10.1038/299121a0

Cornuelle, B. D., Worcester, P. F., Hildebrand, J. A., Hodgkiss, W. S., Jr., Duda, T. F., Boyd, J., et al. (1993). Ocean acoustic tomography at 1000-km range using wavefronts measured with a large-aperture vertical array. *Journal of Geophysical Research*, *98*(C9), 16365–16377. https://doi.org/10.1029/93JC01246

Desbruyères, D., McDonagh, E. L., King, B. A., & Thierry, V. (2017). Global and full-depth ocean temperature trends during the early twenty-first century from Argo and repeat hydrography. *Journal of Climate*, *30*(6), 1985–1997. https://doi.org/10.1175/JCLI-D-16-0396.1

Desbruyères, D. G., Purkey, S. G., McDonagh, E. L., Johnson, G. C., & King, B. A. (2016). Deep and abyssal ocean warming from 35 years of repeat hydrography. *Geophysical Research Letters*, *43*(19), 10356–10365. https://doi.org/10.1002/2016GL070413

D'Spain, G. L., Berger, L. P., Kuperman, W. A., Stevens, J. L., & Baker, G. E. (2001). Normal mode composition of earthquake T phases. In C. de Groot-Hedlin, & J. Orcutt (Eds.),. *Monitoring the Comprehensive Nuclear-Test-Ban Treaty: Hydroacoustics*. (Eds.) (Vol. 158, pp. 475–512). Birkhäuser. https://doi.org/10.1007/978-3-0348-8270-5_4

Dushaw, B. D. (1999). Inversion of multimegameter-range acoustic data for ocean temperature. *IEEE Journal of Oceanic Engineering*, *24*(2), 215–223. https://doi.org/10.1109/48.757272

Dushaw, B. D. (2019). Ocean acoustic tomography in the North Atlantic. *Journal of Atmospheric and Oceanic Technology*, *36*(2), 183–202. https://doi.org/10.1175/JTECH-D-18-0082.1

Dushaw, B. D., Worcester, P. F., Munk, W. H., Spindel, R. C., Mercer, J. A., Howe, B. M., et al. (2009). A decade of acoustic thermometry in the North Pacific Ocean. *Journal of Geophysical Research*, *114*(7), 1–24. https://doi.org/10.1029/2008JC005124

ECCO Consortium. (2021). Synopsis of the ECCO central production global ocean and sea-ice state estimate (p. 17). https://doi.org/10.5281/zenodo.4533349

Fieux, M., Molcard, R., & Morrow, R. (2005). Water properties and transport of the Leeuwin Current and eddies off Western Australia. *Deep-Sea Research Part I: Oceanographic Research Papers*, *52*(9), 1617–1635. https://doi.org/10.1016/j.dsr.2005.03.013

Forget, G., Campin, J. M., Heimbach, P., Hill, C. N., Ponte, R. M., & Wunsch, C. (2015). ECCO version 4: An integrated framework for non-linear inverse modeling and global ocean state estimation. *Geoscientific Model Development*, *8*(10), 3071–3104. https://doi.org/10.5194/gmd-8-3071-2015

Fu, Q., Johanson, C. M., Warren, S. G., & Seidel, D. J. (2004). Contribution of stratospheric cooling to satellite-inferred tropospheric temperature trends. *Nature*, *429*(6987), 55–58. https://doi.org/10.1038/nature02524

Gregory, J. M. (2000). Vertical heat transports in the ocean and their effect on time-dependent climate change. *Climate Dynamics*, *16*(7), 501–515. https://doi.org/10.1007/s003820000059

Hansen, J., Lacis, A., Rind, D., Russell, G., Stone, P., Fung, I., et al. (1981). Climate sensitivity: Analysis of feedback mechanisms. *Climate Processes and Climate Sensitivity*, *29*, 337–351. https://doi.org/10.1029/GM029p0130

Held, I. M., Winton, M., Takahashi, K., Delworth, T., Zeng, F., & Vallis, G. K. (2010). Probing the fast and slow components of global warming by returning abruptly to preindustrial forcing. *Journal of Climate*, *23*(9), 2418–2427. https://doi.org/10.1175/2009JCLI3466.1

Johnson, G. C., Cadot, C., Lyman, J. M., McTaggart, K. E., & Steffen, E. L. (2020). Antarctic Bottom Water warming in the Brazil Basin: 1990s through 2020, from WOCE to Deep Argo. *Geophysical Research Letters*, *47*(18), e2020GL089191. https://doi.org/10.1029/2020GL089191

Kostov, Y., Armour, K. C., & Marshall, J. (2014). Impact of the Atlantic meridional overturning circulation on ocean heat storage and transient climate change. *Geophysical Research Letters*, *41*(6), 2108–2116. https://doi.org/10.1002/2013GL058998

Luyten, J. R., & Roemmich, D. H. (1982). Equatorial currents at semi-annual period in the Indian Ocean. *Journal of Physical Oceanography*, *12*(5), 406–413. https://doi.org/10.1175/1520-0485(1982)012<0406:ECASAP>2.0.CO;2

McPhaden, M. J. (1982). Variability in the central equatorial Indian Ocean. Part I: Ocean dynamics. *Journal of Marine Research*, *40*(1), 157–176.

Munk, W., Worcester, P., & Wunsch, C. (1995). *Ocean acoustic tomography* (p. 433). Cambridge University Press.

Munk, W., & Wunsch, C. (1979). Ocean acoustic tomography: A scheme for large scale monitoring. *Deep-Sea Research, Part A: Oceanographic Research Papers*, *26*(2), 123–161. https://doi.org/10.1016/0198-0149(79)90073-6

Munk, W., & Wunsch, C. (1982). Up–down resolution in ocean acoustic tomography. *Deep-Sea Research, Part A: Oceanographic Research Papers*, *29*(12), 1415–1436. https://doi.org/10.1016/0198-0149(82)90034-6

Munk, W., & Wunsch, C. (1983). Ocean acoustic tomography: Rays and modes. *Reviews of Geophysics and Space Physics*, *21*(4), 777–793. https://doi.org/10.1029/RG021i004p00777

Munk, W. H., & Forbes, A. M. G. (1989). Global ocean warming: An acoustic measure? *Journal of Physical Oceanography*, *19*(11), 1765–1778. https://doi.org/10.1175/1520-0485(1989)019<1765:gowaam>2.0.co;2

Okal, E. A. (2008). The generation of *T* waves by earthquakes. In R. Dmowska. *Advances in geophysics*. (Eds.) (Vol. 49, pp. 1–65). Elsevier. https://doi.org/10.1016/S0065-2687(07)49001-X

Philander, S. G. (1978). Forced oceanic waves. *Reviews of Geophysics*, *16*(1), 15–46. https://doi.org/10.1029/RG016i001p00015

Purkey, S. G., & Johnson, G. C. (2010). Warming of global abyssal and deep Southern Ocean waters between the 1990s and 2000s: Contributions to global heat and sea level rise budgets. *Journal of Climate*, *23*(23), 6336–6351. https://doi.org/10.1175/2010JCLI3682.1

Reppin, J., Schott, F. A., Fischer, J., & Quadfasel, D. (1999). Equatorial currents and transports in the upper central Indian Ocean: Annual cycle and interannual variability. *Journal of Geophysical Research*, *04*(C7), 15495–15514. https://doi.org/10.1029/1999jc900093

Roemmich, D., Alford, M. H., Claustre, H., Johnson, K., King, B., Moum, J., et al. (2019). On the future of Argo: A global, full-depth, multi-disciplinary array. *Frontiers in Marine Science*, *6*, 439. https://doi.org/10.3389/fmars.2019.00439

Roemmich, D., Church, J., Gilson, J., Monselesan, D., Sutton, P., & Wijffels, S. (2015). Unabated planetary warming and its ocean structure since 2006. *Nature Climate Change*, *5*(3), 240–245. https://doi.org/10.1038/nclimate2513

Roemmich, D., & Gilson, J. (2009). The 2004–2008 mean and annual cycle of temperature, salinity, and steric height in the global ocean from the Argo Program. *Progress in Oceanography*, *82*(2), 81–100. https://doi.org/10.1016/j.pocean.2009.03.004

Roemmich, D., & Wunsch, C. (1984). Apparent changes in the climatic state of the deep North Atlantic Ocean. *Nature*, *307*(5950), 447–450. https://doi.org/10.1038/307447a0

Shang, E. C. (1989). Ocean acoustic tomography based on adiabatic mode theory. *Journal of the Acoustical Society of America*, *85*(4), 1531–1537. https://doi.org/10.1121/1.397355

Spiesberger, J. L., Spindel, R. C., & Metzger, K. (1980). Stability and identification of ocean acoustic multipaths. *Journal of the Acoustical Society of America*, *67*(6), 2011–2017. https://doi.org/10.1121/1.384441

The ATOC Consortium. (1998). Ocean climate change: Comparison of acoustic tomography, satellite altimetry, and modeling. *Science*, *281*(5381), 1327–1332. https://doi.org/10.1126/science.281.5381.1327

Volkov, D. L., Lee, S. K., Landerer, F. W., & Lumpkin, R. (2017). Decade-long deep-ocean warming detected in the subtropical South Pacific. *Geophysical Research Letters*, *44*(2), 927–936. https://doi.org/10.1002/2016GL071661

Worcester, P. F., Cornuelle, B. D., Dzieciuch, M. A., Munk, W. H., Howe, B. M., Mercer, J. A., et al. (1999). A test of basin-scale acoustic thermometry using a large-aperture vertical array at 3250-km range in the eastern North Pacific Ocean. *Journal of the Acoustical Society of America*, *105*(6), 3185–3201. https://doi.org/10.1121/1.424649

Wu, W., Zhan, Z., Peng, S., Ni, S., & Callies, J. (2020). Seismic ocean thermometry. *Science*, *1515*(6510), 1510–1515. https://doi.org/10.1126/science.abb9519

Wunsch, C. (1977). Response of an equatorial ocean to periodic monsoon. *Journal of Physical Oceanography*, *7*(4), 497–511. https://doi.org/10.1175/1520-0485(1977)007<0497:ROAEOT>2.0.CO;2

Wunsch, C. (2016). Global ocean integrals and means, with trend implications. *Annual Review of Marine Science*, *8*(1), 1–33. https://doi.org/10.1146/annurev-marine-122414-034040

Wunsch, C., & Heimbach, P. (2007). Practical global oceanic state estimation. *Physica D: Nonlinear Phenomena*, *230*(1–2), 197–208. https://doi.org/10.1016/j.physd.2006.09.040

Wunsch, C., & Heimbach, P. (2014). Bidecadal thermal changes in the abyssal ocean. *Journal of Physical Oceanography*, *44*(8), 2013–2030. https://doi.org/10.1175/JPO-D-13-096.1